PNAS RESEARCH ARTICLE | PHYSICS

Surface tension of cavitation bubbles

Marine Bossert[a,b], I. Trimaille[a], L. Cagnon[c], B. Chabaud[c], C. Gueneau[c], P. Spathis[c], P. E. Wolf[c], and E. Rolley[b,1]

Edited by Pablo Debenedetti, Princeton University, Princeton, NJ; received January 10, 2023; accepted March 5, 2023

We have studied homogeneous cavitation in liquid nitrogen and normal liquid helium. We monitor the fluid content in a large number of independent mesopores with an ink-bottle shape, either when the fluid in the pores is quenched to a constant pressure or submitted to a pressure decreasing at a controlled rate. For both fluids, we show that, close enough to their critical point, the cavitation pressure threshold is in good agreement with the Classical Nucleation Theory (CNT). In contrast, at lower temperatures, deviations are observed, consistent with a reduction of the surface tension for bubbles smaller than two nanometers in radius. For nitrogen, we could accurately measure the nucleation rate as a function of the liquid pressure down to the triple point, where the critical bubble radius is about one nanometer. We find that CNT still holds, provided that the curvature dependence of the surface tension is taken into account. Furthermore, we evaluate the first- and second-order corrections in curvature, which are in reasonable agreement with recent calculations for a Lennard-Jones fluid.

cavitation | surface tension | Tolman length | nucleation

Significance

Millimetric water droplets adopt a spherical shape due to surface tension. The value of this physical parameter is often kept the same to describe smaller droplets, down to the nanometer scale. By studying in detail the cavitation in simple fluids, we show that the simple macroscopic capillarity is indeed relevant for cavitation bubbles as small as 1 nm, provided that the bulk surface tension is corrected in order to take into account the curvature of the bubbles. Once normalized, this correction is similar for helium and nitrogen and in good agreement with predictions for a Lennard-Jones fluid. Our results thus provide a benchmark for using the concept of surface tension for highly curved interfaces.

Cavitation, the formation of a vapor bubble in a metastable liquid below its saturated vapor pressure P_{SAT}, is important in many fields, ranging from engineering (ultrasonic cleaning, propeller damage...) to natural sciences (blocking of sap ascent...). While, for decades, the theoretical framework for cavitation has been the classical nucleation theory (CNT), recent experiments using hexane (1), heptane (2), ethanol (2), argon (3), and nitrogen (4) have shown that measured cavitation rates are many orders of magnitude larger than those predicted by CNT.

This discrepancy is generally attributed to a dependence of the surface tension σ on the interface curvature. Indeed, in the CNT, the liquid–vapor interface is assumed to be infinitely sharp, with a surface tension σ_∞ equal to that for a planar interface, so that the energy barrier for nucleation reads:

$$E_{\mathrm{B}}^{\mathrm{CNT}} = \frac{16\pi}{3}\frac{\sigma_\infty^3}{(P_{\mathrm{V}}-P_{\mathrm{L}})^2}, \quad [1]$$

where P_{V} and P_{L} are the pressures inside and outside the bubble, respectively. In the above experiments, however, the interface thickness is not negligible compared to the nanometric size of the critical nucleus. As a result, the CNT may overestimate the energy barrier, accounting for the measured cavitation rates. The modification of the energy barrier can be computed from density functional models (5). A simpler approach consists in keeping the CNT formalism, in particular Eq. **1**, while allowing the surface tension σ to depend on the radius of curvature R. It was recently demonstrated that such an approach is successful for cavitation in water (6).

To first order in curvature, the dependence of the surface tension is expected to be of the form:

$$\sigma_\infty/\sigma(R) = 1 + 2\delta_\infty/R, \quad [2]$$

(with $R < 0$ for a bubble), as demonstrated a long time ago by Tolman (7). Accordingly, δ_∞ in the above equation is generally called the Tolman length. Beyond first order, it is only recently that many theoretical works have attempted to calculate $\sigma(R)$ for a bubble or a droplet, using direct molecular dynamics simulations (8–10), various density functional calculations (11, 12), or both (13, 14). For Lennard-Jones (LJ) fluids, a consensus has emerged that, first, δ_∞ is negative and of the order of $-0.1d_{\mathrm{LJ}}$ (d_{LJ} is the LJ length scale). Second, as soon as $d_{\mathrm{LJ}}/|R| > 0.1$ which is the case in most nucleation experiments, the second order correction cannot be neglected so that Eq. **2** does not capture the $R-$dependence of σ.

Experimentally testing these predictions through cavitation measurements is a prerequisite for using the concept of an effective surface tension $\sigma(R)$ and the simple

Author affiliations: [a]Institut des NanoSciences de Paris, Sorbonne Université, CNRS, Paris F-75005, France; [b]Laboratoire de Physique de l'Ecole Normale Supérieure, Ecole Normale Supérieure, Université Paris Sciences et Lettres, CNRS, Sorbonne Université, Université de Paris, Paris F-75005, France; and [c]Institut Néel, Université Grenoble Alpes, CNRS, Grenoble F-38042, France

---

Author contributions: M.B., I.T., L.C., B.C., C.G., P.S., P.E.W., and E.R. designed research; M.B., I.T., L.C., B.C., C.G., P.S., and E.R. performed research; M.B., I.T., L.C., B.C., C.G., P.S., P.E.W., and E.R. analyzed data; and M.B., I.T., L.C., B.C., C.G., P.S., P.E.W., and E.R. wrote the paper.

The authors declare no competing interest.

This article is a PNAS Direct Submission.

Copyright © 2023 the Author(s). Published by PNAS. This article is distributed under Creative Commons Attribution-NonCommercial-NoDerivatives License 4.0 (CC BY-NC-ND).

[1] To whom correspondence may be addressed. Email: etienne.rolley@ens.fr.

This article contains supporting information online at http://www.pnas.org/lookup/suppl/doi:10.1073/pnas.2300499120/-/DCSupplemental.

Published April 6, 2023.

and powerful tools of capillarity in situations where the interface is highly curved, ranging from homogeneous nucleation of droplets to sessile nanodroplets (15, 16), meniscii in mesopores (17) or liquid interfaces under an AFM tip (18). Experimental data are however scarce. Interpretation of most cavitation experiments in simple fluids only yields the effective surface tension for a single value of R, equal to the radius R^* of the critical nucleus (3, 4). This single value $\sigma(R^*)$ is not enough to test the validity of Eq. **2** and to determine first- and second-order corrections in curvature. More detailed experiments have been performed in ethanol and water (19, 20). The analysis of the pressure dependence of the cavitation rate points to the relevance of the second-order correction, but its estimate may be specific to these fluids and has been obtained only in a restricted temperature range.

In a recent work, we demonstrated that, by using porous materials made of assemblies of individual pores with an ink-bottle shape, it is possible to accurately measure the cavitation rate of hexane at room temperature and a given liquid pressure in a single shot experiment (1). Here, we extend this new technique to the study of cavitation in two simple cryogenic fluids, helium and nitrogen, over a large range of temperatures. By monitoring the fluid content in the pores when decreasing the liquid pressure, we can determine the cavitation threshold, as well as the cavitation rate around this threshold. At high temperatures, we show that our results are in good agreement with the CNT; in other words, the critical radius is large enough to ensure $\sigma(R) = \sigma_\infty$. At low temperatures, our measurements evidence a decrease of the surface tension, with respect to its bulk value, due to the curvature of the critical bubble. Furthermore, for nitrogen, the optical technique used to monitor the fluid content allows to accurately measure the pressure dependence of the cavitation rate, hence to probe the second-order correction to σ. Using the procedure introduced by Bruot and Caupin (20), we have extracted from the experimental data the first- and second-order contributions to $\sigma(R)$. These contributions are found to be of the same order of magnitude and both are in reasonable agreement with density functional theory (DFT) predictions.

Measurement of the Cavitation Threshold

Cavitation is studied in membranes of porous alumina (1) or porous silicon (21). The native independent pores are roughly cylindrical, with a diameter and a length which can be respectively tuned in the ranges 10 to 50 nm and 1 to 10 μm by varying the synthesis conditions. Their typical volume V_P is of the order of $10^{-21}\,\mathrm{m}^3$ (*Materials and Methods*). In order to obtain the ink-bottle shape necessary for evaporation to proceed by cavitation, the pore aperture is reduced by atomic layer deposition (21).

Cavitation is monitored by measuring sorption isotherms, that is the amount of fluid in the pores as a function of the vapor pressure P_V in the gas reservoir. For nitrogen, we use optical interferometry in white light (WLI) which yields the optical thickness L of the sample. We have checked that the variation of L is proportional to the amount of fluid inside the pores (22). WLI is more precise and less prone to drift than volumetry. While it only probes the illuminated part of the sample, the latter still contains a huge number of pores (of order of 10^9, about one-tenth of their total number).

A typical optical isotherm is shown in Fig. 1, where the difference $\Delta L \equiv L(P_V) - L(P_V = 0)$ is plotted as a function of the vapor pressure P_V. First, P_V is increased up to the saturation pressure P_{SAT} in order to fill the pores. Then, P_V is decreased at a constant rate. In the first step, the optical thickness barely decreases: the liquid–vapor meniscii are pinned at the aperture of the pore and the sample remains saturated with liquid. At some point ($P_V \lesssim 0.8P_{SAT}$ in Fig. 1), ΔL starts to decrease, corresponding to the recession of meniscii in the largest apertures. This recession regime occurs in a wide pressure range as there is some dispersion in the aperture diameters, due to both the initial dispersion in pore diameter and the ALD process. Finally, the sharp decrease of ΔL over a narrow pressure range around $0.67P_{SAT}$ is the signature of cavitation in the pores whose aperture radius is smaller than a temperature-dependent critical value. The cavitation threshold P_V^* is defined as the pressure at mid-height of the cavitation step. Here and below, we use the suffix * for quantities evaluated at this threshold. The corresponding liquid

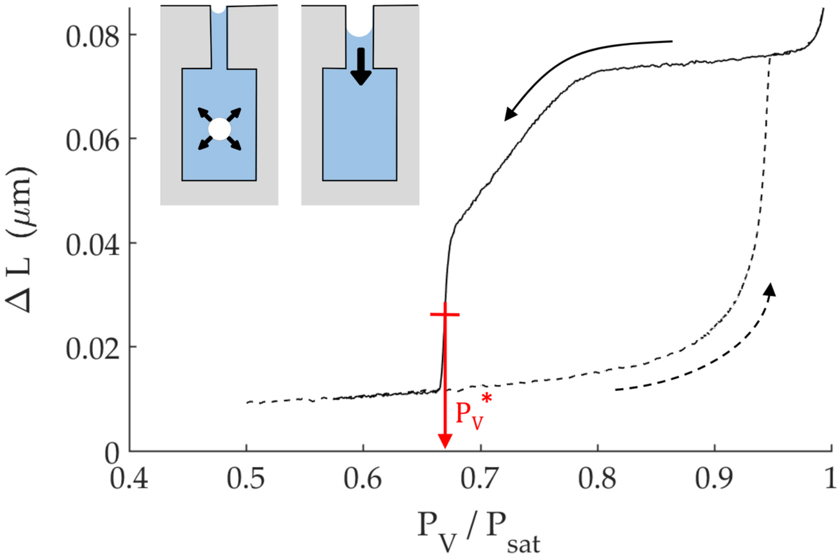

Fig. 1. Nitrogen optical isotherm at 90 K for the porous alumina sample A (mean pore diameter 33 nm, Table 1). Upon decreasing the pressure, meniscii start to recede in the larger apertures at $P_V \simeq 0.8P_{sat}$, until cavitation occurs around $0.67P_{sat}$. Inset: sketch of meniscus receding (*Right*) and cavitation (*Left*) in an ink-bottle pore.

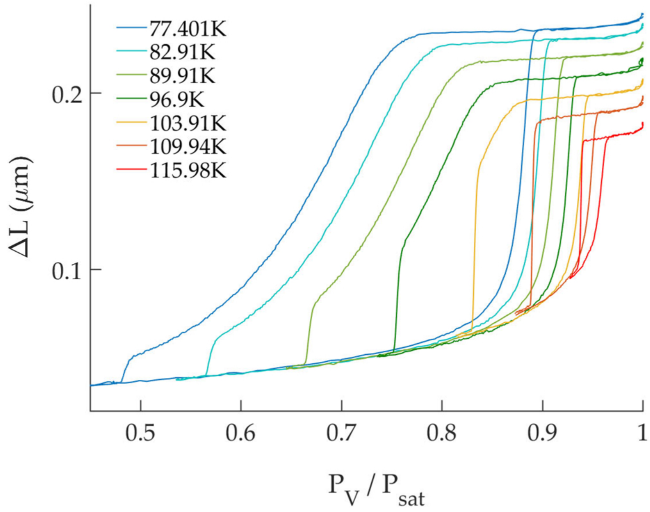

Fig. 2. Nitrogen optical isotherms for the porous alumina sample B (mean pore diameter 19 nm, Table 1). The cavitation pressure and the height of the cavitation step increase with temperature.

pressure at the threshold, P_{L}^*, is derived from phase equilibrium between the vapor and the metastable liquid (*Material and Methods*). Away from the threshold, P_{L}, the liquid pressure inside the pores, is similarly derived from P_{V}. In the following, we will use P_{L} to measure the departure from bulk-phase equilibrium $P_{\mathrm{L}} = P_{\mathrm{SAT}}$.

Such isotherms have been measured for nitrogen in a large temperature range in several porous samples with various pore diameters (Table 1 in *Material and Methods*). Fig. 2 shows a series of isotherms measured on the porous alumina sample B. As the temperature increases, the threshold P_{V}^* and the fraction of pores emptying through cavitation increase. This is due to the temperature variation of σ_∞ which favors cavitation with respect to meniscus recession at high temperature (21).

Similar experiments have been performed for normal liquid helium at temperatures above the superfluid transition ($\simeq$2.17 K). In this case, the adsorbed amount is measured by a continuous volumetric method (21). During evaporation, the cell is pumped through a fixed impedance so that the rate of decrease of P_{V} varies through the cavitation stage: P_{V}^* is then obtained as the pressure where $|\dot{P}_{\mathrm{V}}|$ is minimal (*SI Appendix*).

Surface Tension from Cavitation Threshold

In order to obtain the surface tension at the scale of the critical bubble, we first compute the energy barrier at the cavitation threshold. According to CNT, the nucleation rate $J(P_{\mathrm{L}})$ at a fixed liquid pressure P_{L} is given by

$$J(P_{\mathrm{L}}) = J_0 \exp^{-E_{\mathrm{B}}(P_{\mathrm{L}})/k_{\mathrm{B}}T}, \qquad [3]$$

with J_0 being a prefactor which is controlled by the dynamics of the critical bubble (5, 23). For nitrogen, the pressure is decreased at a constant rate $A = -dP_{\mathrm{L}}/dt$. Assuming that the energy barrier can be linearized as $E_{\mathrm{B}} = E_{\mathrm{B}}^* + \alpha\,(P_{\mathrm{L}} - P_{\mathrm{L}}^*)k_{\mathrm{B}}T$ in the vicinity of the cavitation threshold, the probability $\Sigma(P_{\mathrm{L}})$ that cavitation has not occurred at pressure P_{L} in a pore of volume V_{P} is (*SI Appendix*):

$$\Sigma(P_{\mathrm{L}}) = \exp\left[-\frac{V_{\mathrm{P}}}{A\alpha} J(P_{\mathrm{L}})\right]. \qquad [4]$$

As shown in *Materials and Methods*, $\Sigma(P_{\mathrm{L}})$ =1/2 corresponds to the middle of the cavitation step, i.e., to $P_{\mathrm{L}} = P_{\mathrm{L}}^*$. The energy barrier E_{B}^* at the threshold is thus

$$E_{\mathrm{B}}^* = k_{\mathrm{B}}T \ln\left[J_0 V_{\mathrm{P}}/(A\alpha \ln 2)\right]. \qquad [5]$$

For the volumetric measurements with helium, the flow rate is imposed instead of the pressure ramp and the above expression is modified as

$$E_{\mathrm{B}}^* = k_{\mathrm{B}}T \ln\left[J_0 V_{\mathrm{P}}/\tau\right], \qquad [6]$$

where the characteristic time scale of cavitation, τ, is the duration of the cavitation step (*SI Appendix*).

In Eqs. **5** and **6**, A (or τ) and V_{P} are known. For Eq. **5**, we approximate α by its CNT expression $\left(\partial E_{\mathrm{B}}^{\mathrm{CNT}}/\partial P_{\mathrm{L}}|_T\right)/(k_{\mathrm{B}}T)$. As we will show below, this is correct within 20% (Fig. 6). Since α enters Eq. **5** through a logarithmic factor, our approximation has a negligible impact on E_{B}^*. The last parameter is the prefactor J_0; for our experimental conditions, as usual for a cryogenic liquid not too close to the critical point (3, 4) and for water(6) close to room temperature, the dynamics of the critical bubble is controlled by the viscous flow in the liquid. We use the corresponding expression $J_0 = n_{\mathrm{L}}\frac{\sigma_\infty}{\eta}\left(\frac{\sigma_\infty}{k_{\mathrm{B}}T}\right)^{1/2}(1 - P_{\mathrm{L}}/P_{\mathrm{V}})^{-1}$, where n_{L} is the number density of the liquid and η its viscosity (23) and (5) and *SI Appendix*.

Plugging the above values in Eqs. **5** or **6** yields E_{B}^* in the range of 40 to 55 $k_{\mathrm{B}}T$ for both nitrogen and helium (*SI Appendix*, Fig. S2). Because the experimental parameters V_{P} and A or τ vary from run to run, comparing our results with CNT is easier in terms of the effective surface tension σ which, for a given fluid, should only depend on the temperature and on the radius of the critical bubble. Due to the thickness of the bubble interface, different choices can be used for the bubble radius and for the surface tension (24). When using the so-called stress radius R_{S}^* and the associated surface tension $\sigma(R_{\mathrm{S}}^*)$, for which the Laplace equation $R_{\mathrm{S}}^* = 2\sigma(R_{\mathrm{S}}^*)/(P_{\mathrm{L}}^* - P_{\mathrm{V}}^*)$ is satisfied, the energy barrier is given by the CNT expression (Eq. **1**), provided σ_∞ is replaced by $\sigma(R_{\mathrm{S}}^*)$ (24). Equating this CNT expression to the measured barrier thus yields the effective surface tension:

$$\sigma(T, R_{\mathrm{S}}^*) = \left[\frac{3}{16\pi} E_{\mathrm{B}}^*(P_{\mathrm{V}}^* - P_{\mathrm{L}}^*)^2\right]^{1/3} = \sigma_\infty(T)\left[\frac{E_{\mathrm{B}}^*}{E_{\mathrm{B}}^{\mathrm{CNT}*}}\right]^{1/3}. \qquad [7]$$

The ratio σ/σ_∞ is plotted in Fig. 3 as a function of the normalized radius $|R_{\mathrm{S}}^*|/d_{\mathrm{LJ}}$ as obtained from $\sigma(T, R_{\mathrm{S}}^*)$ and the Laplace equation for both nitrogen and helium, using, respectively, for d_{LJ} the values 0.375 nm and 0.26 nm for nitrogen and helium. For a given fluid, increasing values of R_{S}^* correspond to increasing temperatures, reflecting the fact that σ_∞ decreases when T increases while E_b only weakly depends on T. The plot of σ/σ_∞ as a function of the normalized temperature T/T_{C} can be found in *SI Appendix*, Fig. S4.

Fig. 3 exhibits two important features. First, the surface tension equals its bulk value for large critical bubbles ($|R_{\mathrm{S}}^*|/d_{\mathrm{LJ}} > 10$); this implies that the CNT is valid in this regime and that the evaluation of J_0 is correct. Second, for small bubbles, σ becomes significantly smaller than σ_∞, in agreement with expectation. For nitrogen, the relative deviation reaches -0.2 for $|R_{\mathrm{S}}^*|/d_{\mathrm{LJ}} \simeq 3$, and -0.15 for helium for $|R_{\mathrm{S}}^*|/d_{\mathrm{LJ}} \simeq 5$. Data from earlier cavitation experiments by Baidakov and coworkers in superheated argon (3) and nitrogen (4) can be analyzed

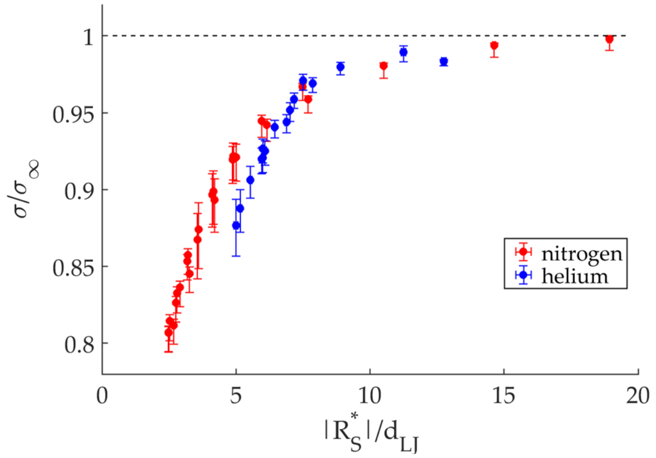

Fig. 3. Normalized surface tension as a function of the normalized bubble curvature $|R^*_S|/d_{LJ}$. Data for helium are measured above the superfluid transition. d_{LJ} for helium and nitrogen are given in the text. The temperature range is 65 to 120 K for nitrogen and 2.3 to 4.5 K for helium. The uncertainty on σ_∞ is about 1% and is not taken into account in the evaluation of the error bars (*SI Appendix*).

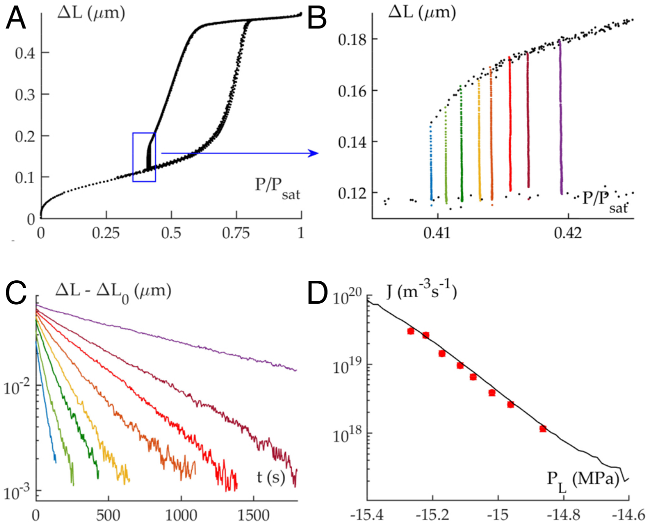

Fig. 4. (*A*) Optical isotherms measured in nitrogen at 73 K on the porous alumina sample C (Table 1) during quenching at various pressures. The total measurement time is about 48 h. (*B*) Close-up of the isotherms showing the relaxations at constant pressures 239.7, 240.36, 241.07, 241.86, 242.41, 243.24, 244.04, and 245.51 mbar. (*C*) Relaxation of $\Delta L - \Delta L_0$ at constant pressures (same values as in *B*). ΔL_0 stands for the optical thickness of empty pores ($\Delta L_0 \simeq 0.12$ µm, a small variation is allowed from run to run to account for the small long-term drift). (*D*) Nucleation rate J as a function of the liquid pressure: from the relaxation time measured in *C* (squares—the size of the symbols sets the uncertainty) and from the shape of the isotherm measured at constant pressure rate (line).

in the same way and yield a decrease of σ for small nucleus consistent with our measurements, though with a much larger scatter (*SI Appendix*, Fig. S7).

We stress that Fig. 3 cannot be used to test Eq. **2** or to determine the respective first- and second-order corrections in curvature. Indeed, in Fig. 3, R^*_S varies together with T, whereas because the Tolman length may depend on temperature[*], a test of Eq. **2** requires varying R^*_S at a fixed temperature. Because $R^*_S = 2\sigma(R^*_S)/(P^*_L - P^*_V)$, this amounts to vary P^*_V. In the following, we achieve this requirement by varying the cavitation rate.

Determination of the Generalized Tolman Length from the Pressure Dependence of the Cavitation Rate

The pressure dependence of the cavitation rate, or that of the energy barrier, $\alpha = (\partial E_B/\partial P_L|_T)/(k_B T)$, can be determined by using two different methods for nitrogen.

Relaxation after Quenching. The first method is similar to the one we previously reported for hexane (1). Starting from a sample fully filled with liquid, it consists in quenching the sample down to a pressure P_L close to P^*_L by decreasing the pressure at a fast rate down to P_L and then closing the cell (*Materials and Methods*). As shown in Fig. 4 *A* and *B*, the optical signal ΔL then decreases with time t to a limiting value ΔL_0 as $\exp(-t/\tau_{\exp})$ (Fig. 4*C*). ΔL_0 reflects the contribution of the fluid adsorbed on the walls of the "emptied" pores at equilibrium and can be accurately determined along the condensation branch of the isotherm (dashed line in Fig. 1), at least when the condensation and evaporation branches are well separated. Close to the cavitation step, the number of filled pores is then proportional to $\Delta L - \Delta L_0$.

As a result, the number of filled pores exponentially decays with the characteristic time $\tau_{\exp}(P_L)$, and the nucleation rate $J(P_L)$ equals $1/(\tau_{\exp} V_P)$. Repeating the experiment at different pressures, we determine the pressure dependence of the nucleation rate. We find that J varies exponentially with P_L (Fig. 4*D*), allowing to compute the value of α through Eq. **3**.

We performed such relaxation experiments at two different temperatures. The corresponding data points for α are shown in red in Fig. 6. This method is simple but requires a very long-term temperature stability. As discussed below, analyzing the shape of a single isotherm provides a more efficient way to determine the value of the parameter α.

Analysis of the Isotherm Shape. The magnification of the cavitation step of Fig. 1 is shown in the *Inset* of Fig. 5. As explained above, after subtracting the contribution ΔL_0 of the fluid adsorbed in empty pores (dashed blue line, measured during condensation), the signal is proportional to the number of filled pores. When the pressure is decreased along the isotherm, this number decreases through two mechanisms, namely cavitation and meniscus recession. Assuming that the cavitation probability does not depend on the aperture size, the ratio Ψ between the actual number of filled pores and the number that would be expected without cavitation at a given pressure is

$$\Psi = \frac{\Delta L_P}{\Delta L_P + \Delta L_V}, \qquad [8]$$

where the optical thicknesses ΔL_P and ΔL_V are defined in Fig. 5. $\Psi(P_L)$ obeys (*Materials and Methods*):

$$\frac{d\Psi}{dP_L} = \frac{J(P_L)V_P}{A}\Psi. \qquad [9]$$

This is exactly the equation obeyed by $\Sigma(P_L)$ (*SI Appendix*, Eq. 6). Hence, $\Psi(P_L)$ is expected to show the characteristic

---

[*] Such a temperature dependence of the Tolman length would naturally explain the difference, for a given normalized radius $|R^*_S|/d_{LJ}$, in σ/σ_∞ between nitrogen and helium, the reduced temperature T/T_C being different for both fluids.

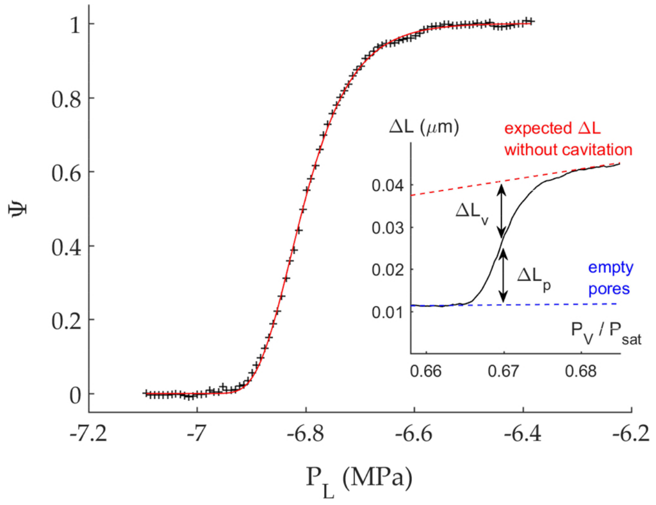

Fig. 5. Fraction Ψ of pores that have not cavitated at pressure P_l: experimental points (crosses) and fit by the double exponential of the Eq. **4** (red solid curve). *Inset*: close-up of the cavitation step of Fig. 1. The dotted curves represent the signal ΔL_0 for "empty" pores (blue) and the extrapolated signal (red) that would be observed without cavitation.

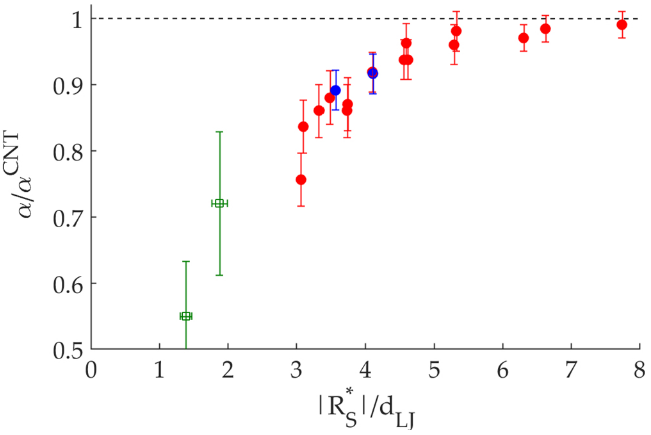

Fig. 6. Plot of $\alpha = \frac{1}{k_\mathrm{b}T}\frac{\partial E_\mathrm{b}}{\partial P_\mathrm{l}}\Big|_T$, normalized by its CNT value calculated from Eq. **1**. Red disks: this work, from the isotherm shape. Blue: this work, from relaxation after quenching. Green open square are data for argon condensation, derived from the work of Sinha et al. (25). Note that argon values for α are plotted as a function of the critical EDS radius R_E since the stress radius R_S cannot be derived from ref. 25.

double-exponential dependence of Eq. **4**. Fig. 5 shows that this is indeed the case, and the fit provides the value of α. The uncertainty on α mainly originates from that on the extrapolated contribution of the meniscus recession.

The result of this analysis can be directly compared to that of the relaxation experiment by computing the nucleation rate $J(P_\mathrm{L}) = (A/V_\mathrm{P})\frac{\mathrm{d}\ln\Psi}{\mathrm{d}P_\mathrm{L}}$ from the corrected isotherm shape $\Psi(P_\mathrm{L})$. As shown in Fig. 4*D*, both methods yield the same curves $J(P_\mathrm{L})$ at $T = 73$ K, which validates our method for correcting the isotherm shape for the contribution of the meniscus recession. The radius dependence of α, normalized by its CNT value, is shown in Fig. 6. Again, we find that the CNT is correct for large bubbles. Moreover, α decreases with $|R_\mathrm{S}|$, the correction reaching 20% for the smallest bubbles. Such a reduction is qualitatively consistent with a reduction of the surface tension at small scales.

For helium, a similar analysis can be used to extract the value of α from the volumetric measurements. However, the uncertainty on α is of order ±10% and we can only conclude qualitatively that the parameter α is smaller than the CNT prediction for small radii (*SI Appendix*). In the following, we thus focus on the results for nitrogen.

Nucleation rate has also been measured for argon in condensation experiments (25, 26). Comparing the nucleation rate J for two different supersaturations $S = P_\mathrm{V}/P_\mathrm{SAT}$ allowed Sinha et al. (25) to estimate the number n^* of atoms in the critical nucleus using the nucleation theorem: $n^* = \partial(\ln J)/\partial(\ln S)|_T$ (27). From this estimate, it is possible to derive α as $\alpha = n^*/n^{*\,\mathrm{CNT}}$. The corresponding values are quite consistent with our measurement for nitrogen bubbles, as shown in Fig. 6.

Generalized Tolman Length. In order to determine the curvature dependence of σ for nitrogen, we use the fact that α can be related to R_E, the radius of the equimolar dividing surface (EDS) defined such that there is no excess mass associated with the interface. The EDS is different from the surface of tension (of radius R_S), though one expects that both surfaces lay in the region of the atomistically diffuse interface. Similarly to other work on nucleation (19, 25, 28), we obtain the equimolar volume V_E^* of the critical nucleus through the nucleation theorem which can be written as ref. 27

$$V_\mathrm{E}^* = \frac{\partial E_\mathrm{B}}{\partial \Delta P}\bigg|_T, \qquad [10]$$

where $\Delta P = P_\mathrm{L} - P_\mathrm{V}$. Applied to a spherical critical bubble of radius R_E, this leads to

$$\frac{4\pi}{3}|R_\mathrm{E}^*|^3 = \alpha\,\frac{1}{1-\rho_\mathrm{V}/\rho_\mathrm{L}}, \qquad [11]$$

where ρ_V and ρ_L are the density of the bulk vapor and liquid phases at the cavitation threshold.

It is customary to call δ the (algebraic) distance between the two surfaces:

$$\delta = R_\mathrm{E}^* - R_\mathrm{S}^*, \qquad [12]$$

δ, rather than δ_∞, is called the Tolman length by some authors. In order to avoid any confusion, we will call below δ the generalized Tolman length. The Tolman length δ_∞ is properly defined as the asymptotic value of δ in the limit of zero curvature. As conjectured by Tolman (7), the natural assumption, which should be valid at least at large radius, is to consider δ as a constant: $\delta \simeq \delta_\infty$. Eq. **2** is valid only at this level of approximation.

One can thus probe the validity of this first-order approximation by computing independently δ from R_E^* and R_S^* on the one hand and, using Eq. **2**, δ_∞ from σ and R_S^* on the other. Although both parameters are found to have the same order of magnitude (about—0.3 d_LJ), δ is significantly smaller than δ_∞ (*SI Appendix*, Fig. S5). This implies that δ cannot be considered as a constant and σ cannot be described by a first-order expansion in curvature. This conclusion makes sense in view of the small radii of cavitation bubbles (2.5 to 10 d_LJ) in the temperature range where α is measured.

Curvature Dependence of the Surface Tension

Our results show the necessity to go beyond the above first-order approximation and to allow for a dependence of δ on curvature. Simulations suggest the following dependence (24):

$$\delta = \delta_\infty + \frac{c}{R_s}. \tag{13}$$

The corresponding expansion of the surface tension reads (29):

$$\frac{\sigma_\infty}{\sigma(R)} = 1 + \frac{2\delta_\infty}{R_s} + \frac{\delta_\infty^2 + c}{R_s^2}. \tag{14}$$

Following Bruot and Caupin (20), it is straightforward to compute the two parameters δ_∞ and c from the knowledge of the energy barrier E_B^* and the radius R_E we refer the reader to ref. 20 for the details of the algebra.

The second-order expansion is more customarily written in a Helfrich form (8, 11, 12, 14):

$$\sigma(R) = \sigma_\infty \left(1 - \frac{2\delta_\infty}{R_s}\right) + \frac{\kappa}{R_s^2}, \tag{15}$$

where κ is the average curvature-elastic modulus, involving both the bending rigidity and the rigidity constant associated with Gaussian curvature. Identification of Eqs. **14** and **15** yields $\kappa = \sigma_\infty(3\delta_\infty^2 - c)$.

The results for nitrogen are summarised in Fig. 7, where we compare the asymptotic Tolman length δ_∞ and the rigidity constant κ as a function of temperature to the predictions of two different DFT calculations for a Lennard-Jones fluid. In the middle of the temperature range, we find $\delta_\infty/d_{LJ} \simeq -0.1$ and $\kappa/\epsilon_{LJ} \simeq -0.8$, in reasonable agreement with the DFT calculations ($\epsilon_{LJ} = 98k_B$ is the LJ characteristic energy scale). Within the experimental uncertainty, κ is constant, consistent with the DFT calculations. On the other hand, $|\delta_\infty|$ seems to increase with temperature in the whole experimental range, a behavior not expected from the DFT.

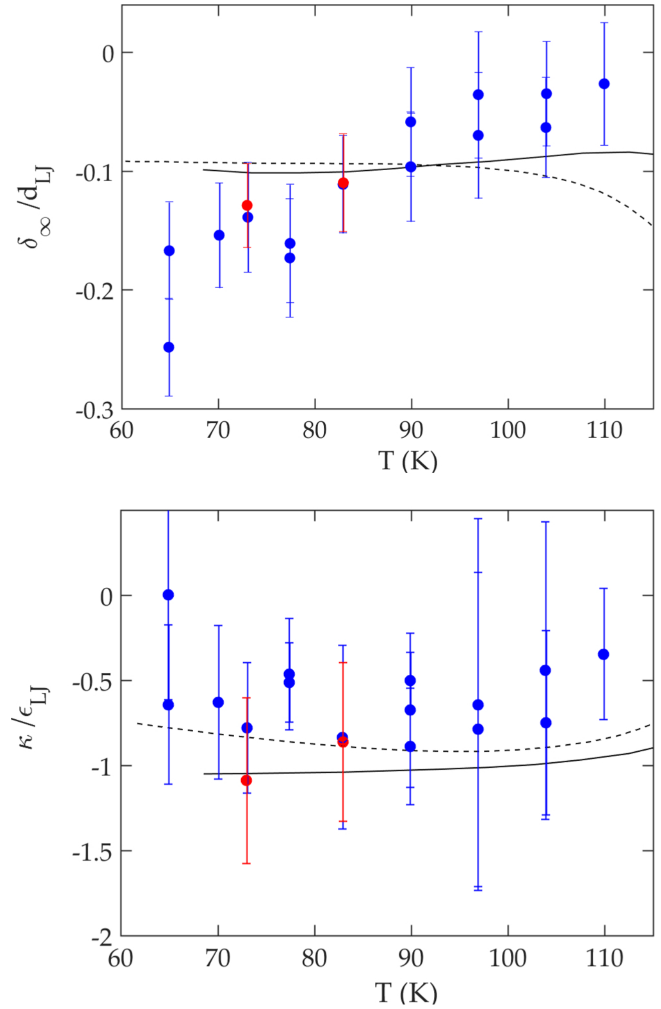

Fig. 7. *Top*: normalized asymptotic Tolman length δ_∞/d_{LJ}. *Bottom*: normalized rigidity constant κ/ϵ_{LJ}. Lines are the results of DFT calculations: full line from ref. 11, dashed line from ref. 12.

We also applied the same analysis to the data that we obtained earlier with hexane at room temperature (1). We find $\delta_\infty/d_{LJ} \simeq -0.15$ and $\kappa/\epsilon_{LJ} \simeq -0.9$, very close to the parameters for nitrogen at the same normalized temperature $T/T_C = 0.57$ (with $d_{LJ} = 0.54$ nm and $\epsilon_{LJ} = 400k_B$ for hexane).

Returning to the surface tension, it turns out that the first- and second-order contributions in Eq. **14** are of similar magnitude over the whole explored temperature range (*SI Appendix*, Fig. S6). Thus, the simple functional form proposed by Tolman $\left(\sigma \propto \frac{1}{1+C^t/R}\right)$ fails to capture the curvature dependence of the surface tension. This seems to be a general feature for nuclei of nanometer size, as the same conclusion has been drawn for ordinary liquids (ethanol, heptane, and water) at room temperature (20).

Conclusion

As a first practical remark, this work demonstrates that continuous measurements of evaporation in a porous material are a powerful tool to investigate cavitation statistics. Here, we have focused on simple fluids, but our technique can be applied to any volatile fluid.

Using nitrogen and helium, we have shown that the classical nucleation theory correctly predicts the cavitation threshold as well as the parameter $\alpha = (1/k_B T)(\partial E_B/\partial P_L|_T)$ when the critical bubbles are large enough, that is at high temperature. At low temperature, for a bubble radius smaller than about 10 times the molecular size, the simple CNT approach is still valid if, instead of the bulk surface tension σ_∞, one uses an effective surface tension $\sigma(R)$. In the range $R/d_{LJ} < 10$, we find that an expansion up to second order in curvature is necessary to account for the experimental results. Presently, the measured values of the Tolman length and rigidity are consistent with DFT but the accuracy of both experiment and calculation is still not high enough to elucidate what happens moderately close to the critical temperature ($T/T_C \sim 0.9$).

To summarize, a macroscopic description of critical cavitation bubbles is quantitatively valid down to the nanometer scale if the surface tension is corrected for the interface curvature. Beyond cavitation, our results give a firmer basis to the concept of an effective surface tension $\sigma(R)$ and suggest that the simple and powerful tools of capillarity can be used in any situations where the liquid–vapor meniscus is highly curved.

Materials and Methods

Samples. Details of the synthesis of the samples can be found in ref. 1 for porous alumina samples and ref. 21 for porous silicon samples. In porous alumina samples, the cylindrical pores are independent with a narrow distribution in diameter. In porous silicon, recent studies (21, 30, 31) have shown that the pore network is more disordered: the pores are still aligned along the etching direction, but constrictions are present along the pores, as well as connections between neighboring pores. The pores size distribution is also quite wide: for the sample used in this work, the mean transverse dimension <d> = 50 nm, with $23 < d < 80$ nm.

Table 1. Characteristics of porous samples

Sample	Mean pore diameter (nm)	Pore length (μm)	R_S^{MAX} (nm)
Porous silicon	50	2	5.5
Porous alumina - A	33	5.4	2.8
Porous alumina - B	19	7	2.2
Porous alumina - C	11	8	1.1
Porous alumina - D	36	85	3.5

For nitrogen experiments, we report only measurements where P_V^* is independent on the pore diameter, so that the fluid–wall interaction is not relevant and the cavitation homogeneous. In practice, we find that this limit is reached when the radius is of the critical nucleus R_S^* is smaller than about one-fifth of the pore diameter (the maximum value R_S^{MAX} of R_S^* is given in Table 1). This limit is also consistent with an earlier study of cavitation in porous silica (32).

For helium, the data discussed in this paper are restricted to temperatures smaller than 4.5 K, corresponding to a R_S^* smaller than 3.5 nm. Based on the theoretical effect of confinement (33), this ensures a negligible influence of confinement on cavitation.

Cell for Optical Measurements with Nitrogen. In contrast to standard volumetric setups, the dead volume around the sample in the optical cell is very large, about 50 cc. This is not an issue because interferometry only probes the fluid content in the pores. Moreover, it has two important advantages: First, it allows to reach the required low-pressure rates with standard flowmeters (Brooks 5850 series). Second, it makes the relaxation experiments at a fixed pressure straightforward: We only need to close the cell once the desired pressure is reached since the subsequent liquid evaporation from the porous sample causes a negligible pressure increase (Fig. 4*B*).

Volumetric Measurements with Helium. Helium cavitation is studied by connecting the experimental cell filled with liquid helium to a vacuum pump through a controllable microvalve and measuring the cell pressure using a room-temperature pressure gauge connected to the cell through a separate 0.2-mm diameter capillary. Thermomolecular effects were computed to be negligible in the range of temperatures and pressures studied, so that the pressure read by the gauge equals the cell pressure. The cavitation isotherm is obtained from the time dependence of this pressure, and an analysis similar to that used above for nitrogen yields the pressure dependence of the cavitation rate (*SI Appendix*).

Calculation of the Liquid Pressure P_L. For a vapor pressure P_L in the vapor reservoir outside the pores, the pressure P_L of the metastable liquid in the pores is calculated assuming that the chemical potentials of the two phases are equal. The chemical potential of the vapor is calculated using the NIST values for fugacity (for nitrogen) or by numerical integration over pressure of the NIST volume data (for helium). The chemical potential of the metastable liquid phase is calculated assuming that the liquid compressibility is equal to the compressibility at saturated vapor pressure. This is consistent with the fact that nucleation occurs far from the spinodal. In principle, the measurement of the optical thickness L on the saturation plateau of the isotherm could be used to determine the metastable liquid compressibility for nitrogen and to check its sensitivity to the confinement (34). However, because we cannot preclude that the L variation is partially due to the emptying of the larger pores, we can only obtain an upper bound for the compressibility (*SI Appendix*). This upper bound is enough to estimate the uncertainty on P_L.

For both nitrogen and helium, the typical effect on P_L of the liquid compressibility is less than 3%, with an uncertainty due to the assumption of a constant compressibility of about 1%.

Equation for $\Psi(P_L)$. Above the cavitation step, the variation dN_R of the number of filled pores due to evaporation by meniscus recession in the pressure interval dP_V is $dN_R = a_V dP_V$, the coefficient a_V being proportional to the slope of the isotherm (red dotted line in Fig. 5). As the cavitation step is very sharp, one can assume that, if cavitation would not occur, the number of pores $N'(P_V)$ remaining filled would be the extrapolation of the behavior above the cavitation step, hence follows the red dotted line, so that $dN' = a_V dP_V$, or in P_L variable, $dN' = a_L dP_L$.

If we now include cavitation, the actual number of filled pores is $N = \Psi N' < N'$. If recession and cavitation are independent processes, the actual number of pores emptying through recession is simply decreased by a factor Ψ: $dN_R = \Psi(a_L dP_L)$. The total number dN of pores emptying through cavitation and recession is thus

$$dN = \left(J(P_L) V_P \frac{N}{A} + a_L \Psi \right) dP_L. \qquad [16]$$

Using this equation to compute the derivative of $\Psi = N/N'$ yields Eq. **9**. Note that the identity with the equation for Σ implies that Σ=1/2 for Ψ=1/2, i.e., the point at midheight of the cavitation step.

Data, Materials, and Software Availability. All study data are included in the article and/or *SI Appendix*.

ACKNOWLEDGMENTS. We thank J. Puibasset for stimulating discussions and careful reading of the manuscript and F. Souris for having developed the experimental cell for helium. This work, including the funding of MB, has been financially supported by Agence Nationale de la Recherche through the project CavConf, ANR-17-CE30-0002.

1. V. Doebele *et al*., Direct observation of homogeneous cavitation in nanopores. *Phys. Rev. Lett.* **125**, 255701 (2020).
2. A. Arvengas, E. Herbert, S. Cersoy, K. Davitt, F. Caupin, Cavitation in heavy water and other liquids. *J. Phys. Chem. B* **115**, 14240–14245, PMID: 21988220 (2011).
3. V. Vinogradov, P. Pavlov, V. Baidakov, Explosive cavitation in superheated liquid argon. *J. Chem. Phys.* **128**, 234508 (2008).
4. V. Baidakov, V. Vinogradov, P. Pavlov, Homogeneous nucleation in liquid nitrogen at negative pressures. *J. Exp. Theor. Phys.* **123**, 629–637 (2016).
5. P. G. Debenedetti, *Metastable Liquids: Concepts and Principles* (Princeton University Press, 1996).
6. G. Menzl *et al*., Molecular mechanism for cavitation in water under tension. *Proc. Natl. Acad. Sci. U.S.A.* **113**, 13582–13587 (2016).
7. R. C. Tolman, The effect of droplet size on surface tension. *J. Chem. Phys.* **17**, 333–337 (1949).
8. A. Van Giessen, E. Blokhuis, Determination of curvature corrections to the surface tension of a liquid-vapor interface through molecular dynamics simulations. *J. Chem. Phys.* **116**, 302–310 (2002).
9. J. G. Sampayo, A. Malijevský, E. A. Müller, E. de Miguel, G. Jackson, Communications: Evidence for the role of fluctuations in the thermodynamics of nanoscale drops and the implications in computations of the surface tension. *J. Chem. Phys.* **132**, 141101 (2010).
10. V. Baidakov, K. Protsenko, Molecular dynamics simulation of cavitation in a Lennard-Jones liquid at negative pressures. *Chem. Phys. Lett.* **760**, 138030 (2020).
11. Ø. Wilhelmsen, D. Reguera, Evaluation of finite-size effects in cavitation and droplet formation. *J. Chem. Phys.* **142**, 064703 (2015).
12. P. Rehner, J. Gross, Surface tension of droplets and Tolman lengths of real substances and mixtures from density functional theory. *J. Chem. Phys.* **148**, 164703 (2018).
13. J. Julin, I. Napari, J. Merikanto, H. Vehkamäki, A thermodynamically consistent determination of surface tension of small Lennard-Jones clusters from simulation and theory. *J. Chem. Phys.* **133**, 044704 (2010).
14. B. J. Block, S. K. Das, M. Oettel, P. Virnau, K. Binder, Curvature dependence of surface free energy of liquid drops and bubbles: A simulation study. *J. Chem. Phys.* **133**, 154702 (2010).
15. D. Shin *et al*., Growth dynamics and gas transport mechanism of nanobubbles in graphene liquid cells. *Nat. Commun.* **6**, 1–6 (2015).
16. S. R. German, M. A. Edwards, Q. Chen, H. S. White, Laplace pressure of individual H2 nanobubbles from pressure-addition electrochemistry. *Nano Lett.* **16**, 6691–6694 (2016).
17. A. L. Donne *et al*., Intrusion and extrusion of liquids in highly confining media: Bridging fundamental research to applications. *Adv. Phys.: X* **7**, 2052353 (2022).
18. S. Kim, D. Kim, J. Kim, S. An, W. Jhe, Direct evidence for curvature-dependent surface tension in capillary condensation: Kelvin equation at molecular scale. *Phys. Rev. X* **8**, 041046 (2018).
19. M. E. M. Azouzi, C. Ramboz, J. F. Lenain, F. Caupin, A coherent picture of water at extreme negative pressure. *Nat. Phys.* **9**, 38–41 (2013).
20. N. Bruot, F. Caupin, Curvature dependence of the liquid-vapor surface tension beyond the Tolman approximation. *Phys. Rev. Lett.* **116**, 056102 (2016).
21. M. Bossert *et al*., Evaporation process in porous silicon: Cavitation vs. pore blocking. *Langmuir* **37**, 14419–14428 (2021).
22. M. Bossert, A. Grosman, I. Trimaille, C. Noûs, E. Rolley, Stress or strain does not impact sorption in stiff mesoporous materials. *Langmuir* **36**, 11054–11060 (2020).
23. M. Blander, J. Katz, Bubble nucleation in liquids. *AIChE J.* **21** (1975).
24. A. Tröster, M. Oettel, B. Block, P. Virnau, K. Binder, Numerical approaches to determine the interface tension of curved interfaces from free energy calculations. *J. Chem. Phys.* **136**, 064709 (2012).

25. S. Sinha, *et al*., Argon nucleation in a cryogenic supersonic nozzle. *J. Chem. Phys.* **132**, 064304 (2010).
26. K. Iland, J. Wölk, R. Strey, D. Kashchiev, Argon nucleation in a cryogenic nucleation pulse chamber. *J. Chem. Phys.* **127**, 154506 (2007).
27. D. Kashchiev, Nucleation work, surface tension, and Gibbs-Tolman length for nucleus of any size. *J. Chem. Phys.* **153**, 124509 (2020).
28. Y. J. Kim, B. E. Wyslouzil, G. Wilemski, J. Wölk, R. Strey, Isothermal nucleation rates in supersonic nozzles and the properties of small water clusters. *J. Phys. Chem. A* **108**, 4365–4377 (2004).
29. V. Baidakov, K. Bobrov, Spontaneous cavitation in a Lennard-Jones liquid at negative pressures. *J. Chem. Phys.* **140** (2014).
30. D. Kondrashova *et al*., Scale-dependent diffusion anisotropy in nanoporous silicon. *Sci. Rep.* **7**, 40207 (2017).
31. M. Thelen, N. Bochud, M. Brinker, C. Prada, P. Huber, Laser-excited elastic guided waves reveal the complex mechanics of nanoporous silicon. *Nat. Commun.* **12**, 3597 (2021).
32. C. J. Rasmussen *et al*., Cavitation in metastable liquid nitrogen confined to nanoscale pores. *Langmuir* **26**, 10147–10157 (2010).
33. F. Bonnet, P. E. Wolf, Thermally activated condensation and evaporation in cylindrical pores. *J. Phys. Chem. C* **123**, 1335–1347 (2019).
34. C. D. Dobrzanski, B. Gurevich, G. Y. Gor, Elastic properties of confined fluids from molecular modeling to ultrasonic experiments on porous solids. *Appl. Phys. Rev.* **8**, 021317 (2021).